Physics of the Earth and Planetary Interiors 366 (2025) 107336

Contents lists available at ScienceDirect

Physics of the Earth and Planetary Interiors

journal homepage: www.elsevier.com/locate/pepi

Modelling geomagnetic jerks with core surface flow derived from satellite gradient tensor elements of secular variation

Frederik Dahl Madsen [a,b,*], Kathryn A. Whaler [a], Ciarán D. Beggan [b], William J. Brown [b], Jonas Bregnhøj Lauridsen [c], Richard Holme [d]

[a] School of GeoSciences, The University of Edinburgh, Grant Institute, James Hutton Road, Edinburgh EH9 3FE, United Kingdom
[b] British Geological Survey, Lyell Centre, Research Avenue South, Edinburgh EH14 4AP, United Kingdom
[c] DTU Space, Technical University of Denmark, Centrifugevej, Building 356, Kongens Lyngby 2800, Denmark
[d] School of Environmental Sciences, The University of Liverpool, Jane Herdman Building, 4 Brownlow St, Liverpool L3 5DA, United Kingdom

ARTICLE INFO

Keywords:
Geomagnetism
Core-surface flow modelling
Geomagnetic jerks
Satellite magnetism

ABSTRACT

The Swarm mission provides along- and across-track differences of magnetic field measurements, making it possible to generate spatial gradients of the geomagnetic field and its secular variation (SV). Similar data are obtainable from the CHAMP mission by taking along-track differences. These can be combined into a spatial gradient tensor of SV. We compare core-surface flow inversions from vector and tensor datasets, with a particular focus on the equatorial geomagnetic jerks observed by the CHAMP and Swarm missions. Our models are obtained directly from the SV data, without relying on numerical simulations for prior information or enforcing any flow geometry. We develop three different flavours of model, all damped to minimise spatial complexity and acceleration between epochs, and find all provide good fits to the data. With these, we scrutinise the extent of equatorial asymmetry required by core-surface flow to fit the data, and relate the flow to observations of changes in length-of-day.

We find that using spatial gradients for flow-inversions improves the spatial resolution compared to using vector measurements, resolving ~1.4 times as many flow coefficients for the Swarm models and ~1.2 for the CHAMP models.

During the 2017 and 2020 Pacific region geomagnetic jerks, our models show pulses in azimuthal flow acceleration, time-centred between the two jerks, and a new pulse occurring in mid-2022. This suggests that a new geomagnetic jerk in this region will occur at the end of 2024. We propose that the observed azimuthal acceleration pulses may occur when previously hypothesised Alfvén wave-packets interact with flow at the surface of the core.

1. Introduction

The geomagnetic field is generated by the complex motion of electrically conducting liquid iron alloy in the outer core. Powered by the geodynamo, the magnetic field constantly changes through this motion, making the geomagnetic field a dynamic and chaotic system (Gubbins and Roberts, 1987). Given that the change of the geomagnetic field on monthly to centennial timescales, known as secular variation (SV), is dominated by advective fluid flow, it is possible to infer some information about flow structures in the core (e.g. Holme, 2015). Earlier core surface flow studies have either used time series of globally distributed ground observatory data (e.g. Beggan and Whaler, 2008; Whaler et al., 2016) or observatory-based SV models (e.g. Finlay and Jackson, 2003) to invert for the flow; however, these are poorly geographically distributed. Satellite magnetic field data from low Earth orbit, on the other hand, offer near-global coverage. With the European Space Agency's Swarm mission (Friis-Christensen et al., 2006), we are able to obtain the magnetic field vector from low Earth orbit, and also the spatial gradient from across- and along track differences, which are more sensitive to changes in the magnetic field and SV (Kotsiaros and Olsen, 2014). Geomagnetic virtual observatories (GVOs; Mandea and Olsen, 2006) can be created from satellite data to create a time series of the magnetic field, its spatial components, and its time derivative, at a given point at satellite altitude, similar to any ground observatory.

* Corresponding author at: School of GeoSciences, The University of Edinburgh, Grant Institute, James Hutton Road, Edinburgh EH9 3FE, United Kingdom.
E-mail address: f.d.madsen@sms.ed.ac.uk (F.D. Madsen).

https://doi.org/10.1016/j.pepi.2025.107336
Received 1 November 2024; Received in revised form 14 February 2025; Accepted 6 March 2025
Available online 11 March 2025

Whereas ground observatories have a spatial bias, the GVO method, further improved by Hammer et al. (2021, 2022), yields equally spaced virtual observatories across the globe.

Typically, global SV varies smoothly over decades. However, sometimes relatively rapid changes occur on the timescale of several months to a year that interrupts the steady progression. These rapid changes in SV are known as geomagnetic jerks (e.g. Courtillot et al., 1978; Brown et al., 2013). They are often spatially and temporally localised, though may be observed at different times around the globe and in different components due to the non-uniform weakly conducting mantle (Backus, 1983; Pinheiro and Jackson, 2008). The origin and dynamics of geomagnetic jerks are still debated. Analysis of observatory data has shown that jerks are primarily of internal origin (Malin and Hodder, 1982). Some studies suggest that jerks are by-products of changes to the core surface flow associated with exchanges in angular-momentum between the core and the mantle (e.g. Duan and Huang, 2020), whereas numerical simulations of the geodynamo have suggested that jerks may be caused by buoyancy release of magnetohydrodynamic wave-packets from the inner core, interacting with the observed field at the core surface (Aubert and Finlay, 2019; Aubert et al., 2022). Geomagnetic jerks are often identified as "V" shapes in geomagnetic SV records from ground observatory measurements (e.g. Courtillot et al., 1978; Mandea et al., 2010; Brown et al., 2013), but can also be identified in satellite data. The 21$^{\text{st}}$ century has seen a sequence of equatorially centred geomagnetic jerks. Jerks have been recognised in the Atlantic region in 2003.5, 2007, and 2011 (e.g. Chulliat and Maus, 2014), in both the Pacific and Atlantic regions in 2014 (Torta et al., 2015), and in the Pacific in 2017 (e.g. Kloss and Finlay, 2019; Finlay et al., 2020) and 2020 (e.g. Pavón-Carrasco et al., 2021). Nearly all of these jerks – the exceptions being the 2011 and 2014 jerks – were observed by the high data-quality satellites CHAMP (2001−2010) and Swarm (2014–).

We investigate the flow associated with equatorial jerks, by inverting SV tensor data created from four-monthly mean GVO spatial gradients from the CHAMP and Swarm satellites for global flow models. After first presenting the Methods (Section 2) and Data (Section 3), we quantify, in Section 4.1, the spatial resolution improvement from using spatial gradient tensor measurements for flow modelling, over using traditional vector measurements. We then create three different types of flow, all regularised to minimise acceleration and spatial complexity, with different imposed assumptions to investigate how the flow evolves in each case. The first flow is otherwise spatiotemporally unconstrained. In the second flow, equatorial symmetry is encouraged (but not enforced), in an attempt to investigate to what extent departures from equatorial symmetry are required to fit the data. Our third flow has relaxed temporal damping on the flow coefficients that correspond to zonal variations such as torsional oscillations (TOs) (e.g. Zatman and Bloxham, 1997; Bloxham et al., 2002; Whaler et al., 2016; Teed et al., 2019). From these flow coefficients, it is possible to calculate the length-of-day contribution from the geostrophic parts of the core-surface flow (Jault et al., 1988; Jault and Finlay, 2015). We find the minimum amount of equatorial antisymmetry required to fit the data in Section 4.2, and examine the temporal evolution of all our flow models in Section 4.3. Then, we investigate the extent to which relaxing the temporal constraint on flow coefficients associated with TOs provides a flow that fits observations of changes in the length-of-day in Section 4.4. Finally, we use all three models to investigate the 2003, 2007, 2017 and 2020 geomagnetic jerks, in Section 4.5. These results are discussed in Section 5 and we conclude in Section 6.

2. Methods

The geomagnetic field, generated in the outer core, is linked to the flow at the surface of the core through the reduced induction equation, assuming negligible diffusion (e.g. Roberts and Scott, 1965):

$$\dot{B}_r + \nabla_{\mathbf{H}}\cdot(\mathbf{u}_{\mathbf{H}} B_r) = 0, \tag{1}$$

where B_r is the radial magnetic field, $\dot{B}_r = \frac{\partial B_r}{\partial t}$ is its time derivative, $\mathbf{u}_{\mathbf{H}}$ is the horizontal velocity, and $\nabla_{\mathbf{H}} = \nabla - \hat{\mathbf{r}}\cdot\nabla$ only contains horizontal derivatives. Assuming that the measured geomagnetic field on the core surface is of internal origin, we can consider $\mathbf{B}$ as the gradient of a potential field, V, outside of the source region:

$$\mathbf{B} = -\nabla V(r,\theta,\phi), \tag{2}$$

where r, θ, and ϕ are spherical polar coordinates radius, colatitude, and longitude, respectively. Commonly this potential field is then represented in spherical harmonics as:

$$V(r,\theta,\phi,t) = a\sum_{n=1}^{N_B}\sum_{m=0}^{n}\left(\frac{a}{r}\right)^{n+1}\left(g_n^m(t)\cos m\phi + h_n^m(t)\sin m\phi\right)P_n^m(\cos\theta) \tag{3}$$

where $P_n^m(\cos\theta)$ are Schmidt quasi-normalised associated Legendre functions of degree and order n and m, respectively, $a = 6371$ km is the reference radius of the Earth, and g and h are weights, known as Gauss coefficients, which are dependent on time, t. We truncate the magnetic field to degree $N_B = 14$ due to contamination at the Earth's surface from the static crustal field at higher degrees (e.g. Cain et al., 1989). Traditionally, to describe the advective core-surface flow, we decompose the flow into its toroidal and poloidal parts (Roberts and Scott, 1965). This is only possible under the assumption that the flow is incompressible, such that $\nabla\cdot\mathbf{u} = 0$ (see e.g. reviews by Gubbins and Roberts, 1987; Holme, 2015). The flow at the core-mantle boundary (CMB), where $u_r = 0$, thus takes the form:

$$\mathbf{u}_{\mathbf{H}} = \nabla\times(\mathscr{T}\mathbf{r}) + \nabla_H(\mathscr{S}\mathbf{r}) \tag{4}$$

where $\mathscr{T}$ and $\mathscr{S}$ are the toroidal and poloidal scalar potentials, respectively. Similarly, these can be represented in terms of spherical harmonics:

$$\begin{aligned}\mathscr{T}(\theta,\phi,t) &= \sum_{n=1}^{N_u}\sum_{m=0}^{n}\left(t_n^{m\,c}(t)\cos m\phi + t_n^{m\,s}(t)\sin m\phi\right)P_n^m(\cos\theta)\\ \mathscr{S}(\theta,\phi,t) &= \sum_{n=1}^{N_u}\sum_{m=0}^{n}\left(s_n^{m\,c}(t)\cos m\phi + s_n^{m\,s}(t)\sin m\phi\right)P_n^m(\cos\theta)\end{aligned} \tag{5}$$

Here, $t_n^{m\,c,s}$ and $s_n^{m\,c,s}$ are the spherical harmonic coefficients for toroidal and poloidal flow, respectively. By truncating the velocity fields at degree N_u, it is assumed that the energy of the flow is constrained within the length-scale related to N_u. This can be considered the "traditional" method of decomposing core-surface flow (e.g. Whaler, 1986; Gubbins and Roberts, 1987; Jackson, 1997; Pais and Jault, 2008; Beggan and Whaler, 2009; Amit and Pais, 2013; Holme, 2015; Whaler et al., 2022), whereas different approaches for obtaining core-surface flow from data have been used. Some researchers expand their models to account for diffusion (e.g. Voorhies, 1993; Metman et al., 2019, 2020). Others model both large-scale advective flow, diffusion, and the small-scale flow (i.e., flow with a spatial scale smaller than that related to N_u), including using data-assimilation with numerical simulations of the geodynamo (e.g. Eymin and Hulot, 2005; Gillet et al., 2015; Kloss and Finlay, 2019; Huder et al., 2019; Gillet et al., 2022; Ropp and Lesur, 2023; Istas et al., 2023; Gillet et al., 2024; Suttie et al., 2025). We also note it is possible to model flow without expanding into a spherical harmonic basis. Livermore et al. (2017) neglected the existence of an inner core to derive an expression for core-flow as a stream function in cylindrical polar coordinates, and Schwaiger et al. (2023) decompose their flow into quasi-geostrophic stream functions to yield local azimuthal and meridional velocity components.

We relate SV at the CMB to the flow by substituting Eqs. (2) and (3), their time derivatives, and Eq. (4), into Eq. (1) (e.g. Roberts and Scott, 1965; Whaler, 1986). After some manipulation, this results in the relation

$$\dot{\mathbf{g}} = \mathbf{Et} + \mathbf{Gs}, \tag{6}$$

where vectors $\dot{\mathbf{g}}$, $\mathbf{t}$, and $\mathbf{s}$ respectively contain the SV, toroidal, and poloidal velocity coefficients, and matrices $\mathbf{E}$ and $\mathbf{G}$ depend on the main field coefficients and the Elsasser and Gaunt integrals, respectively (Gibson and Roberts, 1969; Whaler, 1986). Here, we assume that the magnetic field is known, and use the CHAOS-7.18 geomagnetic field model spherical harmonic coefficients up to degree 14 (Finlay et al., 2020).

We can also relate the Gauss SV coefficients to SV data by taking the first time derivative of V:

$$\dot{\mathbf{d}} = \mathbf{Y}\dot{\mathbf{g}} \tag{7}$$

where $\dot{\mathbf{d}}$ is the data vector, containing the SV GVO data, and elements of $\mathbf{Y}$ contain spherical harmonics and their derivatives. The matrix $\mathbf{Y}$ will have different elements for models based on vector data (e.g. Whaler, 1986) or spatial gradient SV tensor data (e.g. Kotsiaros and Olsen, 2014; Whaler et al., 2022). We link the SV data to the flow coefficients by substituting Eq. (7) into Eq. (6):

$$\dot{\mathbf{d}} = \mathbf{YEt} + \mathbf{YGs} \equiv \mathbf{Am} \tag{8}$$

where $\mathbf{A}$ is the equations of condition matrix, mapping the model vector to the SV data, and $\mathbf{m}$ is the model vector, containing the toroidal and poloidal flow coefficients. Solving this equation, whilst acknowledging the ill-determined nature of the problem, lends itself to a regularised least-squares solution. We follow the approach of Whaler et al. (2016) where data from multiple epochs are inverted simultaneously, regularising the solution both temporally and spatially. We choose our temporal regularisation in order to minimise flow acceleration. For the spatial regularisation, we choose the 'strong norm', originally proposed by Bloxham (1988), which minimises the second spatial derivatives of the flow, averaged across the CMB, thus penalising spatial complexity:

$$\int_{\Omega}\left(\left(\nabla_{\mathrm{H}}{}^{2}u_{\theta}\right)^{2} + \left(\nabla_{\mathrm{H}}{}^{2}u_{\phi}\right)^{2}\right)\mathrm{d}\Omega, \tag{9}$$

where (u_θ, u_ϕ) are meridional and azimuthal flow components, respectively, and Ω is the CMB (e.g. Bloxham, 1988).

The regularised least-squares solution to Eq. (8) thus takes the form

$$\widehat{\mathbf{m}} = \left(\mathbf{A}^{T}\mathbf{C_e}^{-1}\mathbf{A} + \lambda_v\mathbf{C_m}^{-1} + \lambda_t\mathbf{D}^{T}\mathbf{D}\right)^{-1}\mathbf{A}^{T}\mathbf{C_e}^{-1}\dot{\mathbf{d}} \tag{10}$$

where $\mathbf{C_e}$ is the data covariance matrix, which consists of 6×6 or 3×3 data covariance matrices for each GVO location with the variance of each gradient or vector datum arranged along the diagonal, respectively, and zeroes elsewhere. $\mathbf{C_m}$ is the *a priori* model covariance matrix, in this case based on the strong norm, λ_v and λ_t are the spatial and temporal damping factors, respectively, and $\mathbf{D}$ links successive epochs to impose the temporal constraint (see Whaler et al., 2016).

From this methodology, we create three different types of flow model. The first is exactly as described above, regularised in space and time. We refer to them as our minimum acceleration models or minimum acceleration flows. For our second model, we wish to investigate the level of equatorial asymmetry required to fit the data. This will allow us to examine if any important features of the flow are lost when assumptions which enforce equatorial symmetry are employed, such as tangential geostrophy (Holme, 2015). We do this by spatially damping the equatorially symmetric and antisymmetric flow coefficients differently, thus yielding two spatial damping parameters; λ_v^{asymm} and λ_v^{symm}, which act on different elements in the matrix $\mathbf{C_m}$. We experimented with λ_v^{asymm} and λ_v^{symm} to obtain minimal equatorial antisymmetry, while keeping a comparable model root-mean-squared (rms) data misfit to our minimum acceleration models and retaining a similar amount of spatial complexity. By setting up the spatial damping such that the flow is predominantly equatorially symmetric, where equatorial asymmetry is heavily penalised but not forced to be zero, the best solution will reveal the areas of the core-surface flow where equatorial asymmetry is required. In these models, the temporal damping is the same on all flow parameters. We refer to these as symmetric-asymmetric flows, or SA flows.

Finally, we explored whether we could create a flow-model which would fit observations in length-of-day variations (ΔLOD) data as well as geomagnetic observations. Whaler et al. (2016) found that by removing the temporal damping on the flow-coefficients associated with torsional oscillations, their flows could better reproduce ΔLOD observations. Therefore, following their methodology, we relax the temporal damping on the odd degree, zonal toroidal coefficients, again yielding two damping parameters, λ_t^{zt} and λ_t^{nzt}, where λ_t^{zt} damps the odd-degree, zonal toroidal coefficients and λ_t^{nzt} damps all other flow coefficients. The choice of λ_t^{zt} and λ_t^{nzt} was made to obtain the best fit to ΔLOD observations, while still yielding a comparable rms data misfit to our minimum acceleration models. Here, the spatial damping is applied to all flow coefficients with the same damping parameter as for the minimum acceleration model. We refer to these as our TO-like flows.

3. Data

We create 4-monthly spatial gradient tensor SV data and error estimates, at 300 geomagnetic virtual observatories (GVOs), following the method of Hammer et al. (2022), and obtain the 4-monthly vector SV GVO data from the Swarm DISC server (see Data Availability for access to vector data). The vector data were created according to Hammer et al. (2021). Error estimates for each GVO vector or tensor element are computed using the variance of residuals between the GVO datum and the CHAOS 7.18 model estimate of the vector or tensor element at the GVO location, as outlined by Hammer et al. (2021, 2022). Note the number of data changes in each GVO bin on a 4-monthly basis. We use GVO vector data time series from CHAMP for 2001.0–2010.0 and from Swarm for 2014.67–2023.33. The gradient datasets are slightly misaligned with the vector data: We have gradient data for the epochs 2001.67–2010.33 and 2014.33–2024.00 for CHAMP and Swarm, respectively. We invert all the data simultaneously for a temporally varying flow, separately for the CHAMP and Swarm missions, and separately for vector and spatial gradient tensor data. Consequently, the temporal parametrisation of the flow coefficients is the same as that of the GVO data, that is, 4-month snapshots with the temporal damping minimising the differences in flow between subsequent epochs.

Fig. 1 shows the GVO locations, as well as the radial gradient of the radial SV, $\dot{B}_{rr}$, at each GVO for CHAMP (Fig. 1a) and Swarm (Fig. 1b). In Fig. 1a, we see the distinct V-shaped signatures in the equatorial Atlantic region from 2001 to 2010, specifically between longitudes 60°W and 60°E and latitudes ±30°. Although there has not been a formal analysis of how jerks appear in spatial gradients of SV, we see that inflections in the spatial gradients are contemporaneous with inflections in the vector components (Fig. 2), which we recognise as jerk signatures (e.g. Courtillot et al., 1978; Brown et al., 2013; Holme, 2015; Hammer et al., 2022). We therefore interpret these inflections in $\dot{B}_{rr}$ as the spatial gradients signature of the 2003.5 and 2007 jerks. At other longitudes in this period, particularly in the Pacific Ocean, there is very little change to the SV trend. The opposite can be seen in the data from the Swarm period in Fig. 1b. Two jerks are very clear in the equatorial Pacific, most notably between longitudes 150°E and 130°W, although some jerk signature is observed at latitudes as high as 45°N around continental Asia. The Pacific jerks occur in 2017 and 2020 (Pavón-Carrasco et al., 2021; Hammer et al., 2022). It is clear from Fig. 1 that the Swarm data are less noisy than those of CHAMP.

4. Results

We use the conjugate gradient algorithm with Jacobi precondition-

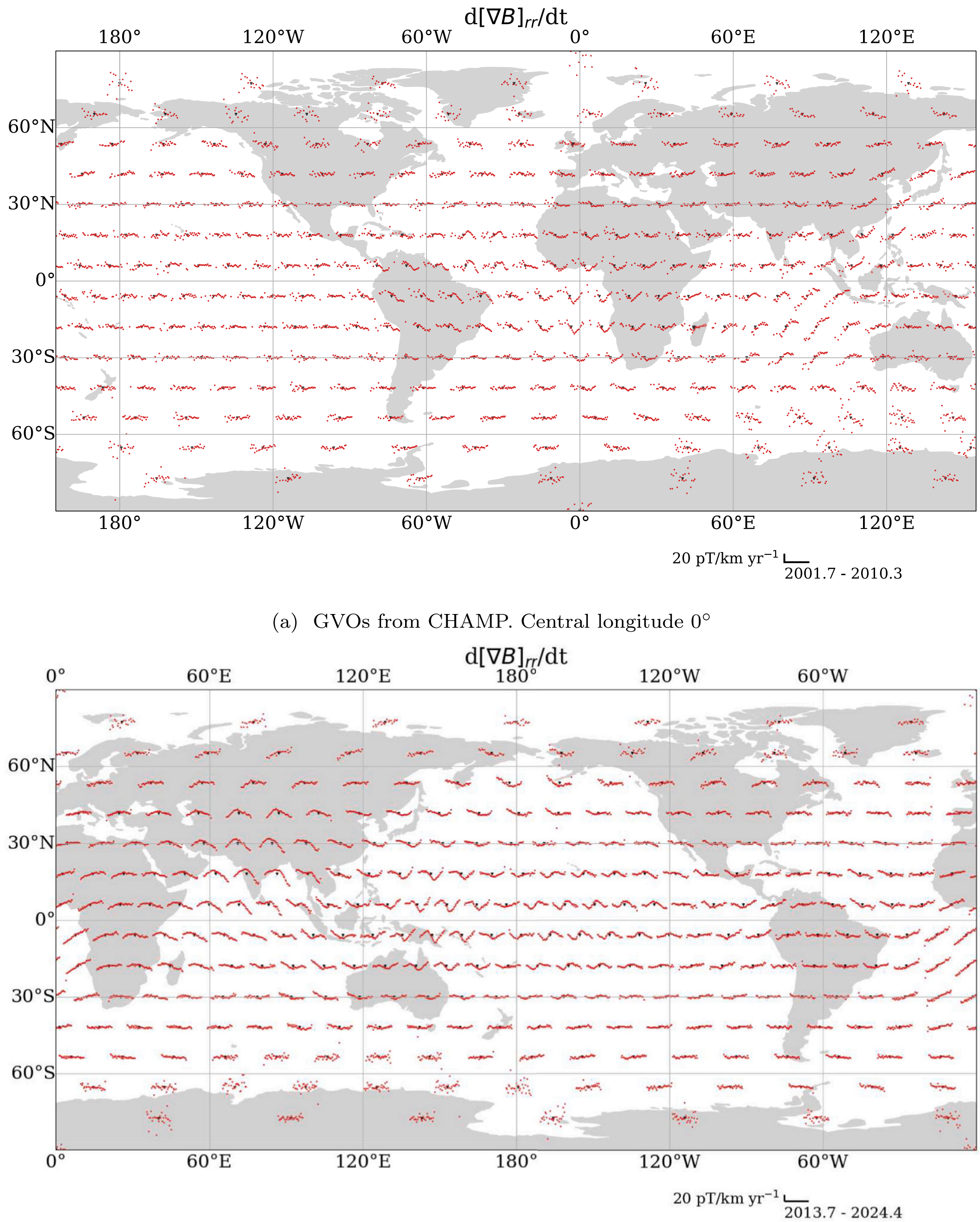

(a) GVOs from CHAMP. Central longitude 0°

(b) GVOs from Swarm. Central longitude 180°.

Fig. 1. Radial derivative of radial SV (red) from CHAMP (a) and Swarm (b) at each GVO (black dots). Data for each GVO are centred on the GVO location. x- and y-axes for each GVO are provided in the bottom right of each figure. Note that (a) is centred on the Atlantic, and (b) is centred on the Pacific. Both plots are in Plate Carrée projection. (For interpretation of the references to colour in this figure legend, the reader is referred to the web version of this article.)

ing to calculate the solution to Eq. (10), first with the spatial gradient data, and then the vector data, for core-surface flow. We truncate both flow and SV at spherical harmonic degree $N_B = N_u = 14$, and find that this is sufficient to ensure convergence of the spherical harmonic expansions of the flow potentials. The spatial damping for the models is based on the tradeoff between the spatial norm and rms misfit, normalised by the data uncertainties, and where possible, to yield comparable rms misfits to the data across the CHAMP- and Swarm-based models. This was not possible for the CHAMP vector data, without grossly overfitting them. The spatial and temporal damping parameters and rms misfits are given in the Supplementary Tables B.1– B.3 for each model. For the sake of comparing flow pairs, the temporal damping for the SA flow is the same as for the minimum acceleration flow, and the spatial damping for the TO-like flows is the same as for the minimum acceleration flows for the same reason. Generally, the models derived from gradient-tensor data yield a significantly lower normalised rms misfit than those derived from vector data. Furthermore, comparing the misfits from CHAMP and Swarm vector data, the Swarm-based models yield a lower misfit than the CHAMP-based models. Similarly, the Swarm gradient data required less damping than their CHAMP counterparts to yield an rms misfit of 1.

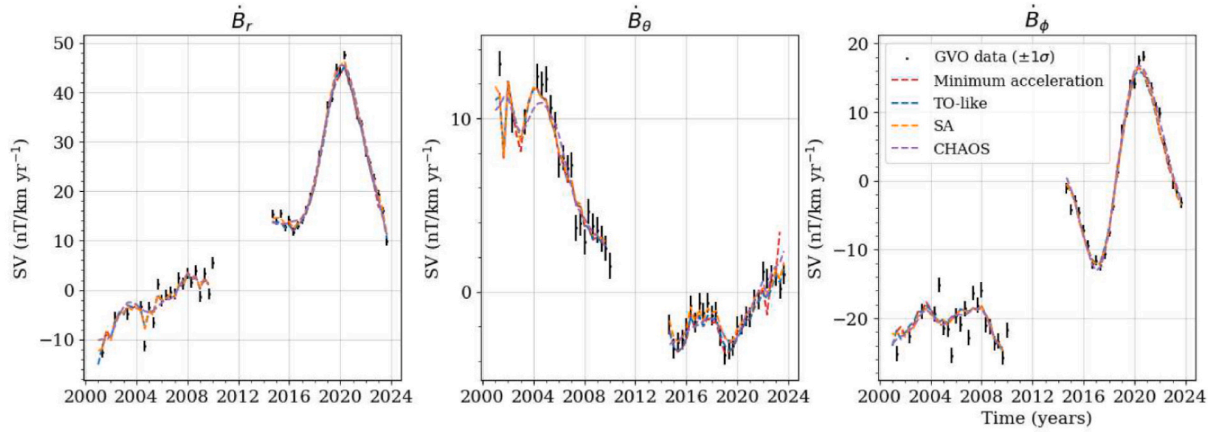

(a) Vector SV.

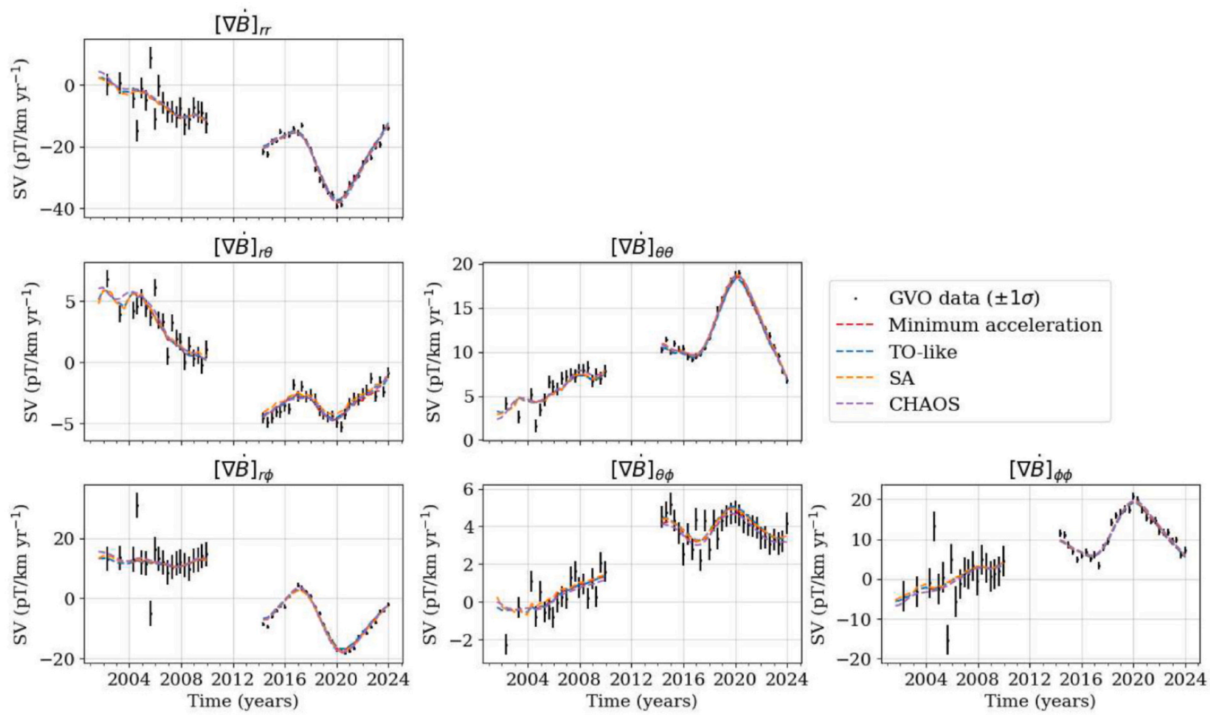

(b) Gradient tensor SV.

Fig. 2. Data and model predictions from vector (a) and gradient tensor (b) measurements from a GVO in the equatorial West Pacific (6.0°N, 164.4°E). Red, blue, and orange correspond to SV predictions from the minimum acceleration, TO-like, and SA models, respectively, and purple line shows predictions of the CHAOS-7.18 magnetic field (Finlay et al., 2020). (For interpretation of the references to colour in this figure legend, the reader is referred to the web version of this article.)

4.1. Model performance and resolution

Fig. 2 shows SV predictions of a set of models of core flows at an equatorial GVO in the West Pacific. We see that for both CHAMP and Swarm, the vector- and gradient tensor-based models fit the data closely, and are in good agreement with the CHAOS-7.18 model (Finlay et al., 2020, shown for reference). For CHAMP, the scatter of the vector data, particularly in the $\dot{B}_\phi$ direction, is larger. This affects the model prediction by yielding sharp changes between the epochs where the data uncertainties are greatest. Several epochs between 2002 and 2005 lack data in this region (due to enhanced solar activity), resulting in the models not capturing the 2003 jerk particularly well. Compared with the CHAMP data, the Swarm data have much lower uncertainties. We see that the flow models resolve both the 2017 and 2020 jerks very well in nearly all components. We attribute the data-points that deviate from both our model estimates and the CHAOS-7.18 estimates to external field contamination. Where the data appear most scattered, the magnitude is actually small, e.g. $\left[\nabla\dot{B}\right]_{r\theta}$ and $\left[\nabla\dot{B}\right]_{\theta\phi}$. Thus our model fits are unbiased for both the vector and gradient tensor data (all models yield histograms of the residuals that are symmetric around a mean which is lower than the data variance), with only a slight underestimate in amplitude, due to the damping.

We formally investigated the spatial resolution of our models, using the minimum acceleration models as examples. We did this first by producing resolution matrices for our flows. The resolution matrix shows how well our inversion is able to resolve the flow coefficients. Following Bloxham et al. (1989), the resolution matrix for our inversion is given by

$$\mathbf{R} = \left(\mathbf{A}^T\mathbf{C_e}^{-1}\mathbf{A} + \lambda_v\mathbf{C_m}^{-1} + \lambda_t\mathbf{D}^T\mathbf{D}\right)^{-1}\mathbf{A}^T\mathbf{C_e}^{-1}\mathbf{A}, \tag{11}$$

which we extend here to include the temporal damping. $\mathbf{R}$ describes the relationship between the real and estimated model parameters, $\mathbf{m}$ and $\widehat{\mathbf{m}}$, respectively, by $\widehat{\mathbf{m}} = \mathbf{R}\mathbf{m}$. Therefore, the ideal resolution matrix is the identity matrix and will have a trace equal to the number of flow parameters, which in our case is 224 for both the toroidal and poloidal flow parts, yielding 448 parameters in total. Diagonal elements deviating from unity show that amplitudes of flow coefficients are not properly recovered, and non-zero off-diagonal elements indicate correlated flow coefficients. By including the temporal damping in Eq. (11), we found that the off-diagonal elements were less prominent than where the temporal damping is omitted from Eq. (11), as investigated by Whaler et al. (2016). We also obtain a smaller trace by including the temporal damping, but found that the higher-degree diagonal elements are larger than when the temporal damping is omitted, suggesting better resolution of smaller length scale features of the flow. We show a comparison between including and excluding the temporal damping in Fig. B.1.

The resolution matrices for snapshots of the flow (2005.33 for CHAMP and 2018.67 for Swarm) are given in Fig. 3 for the vector and spatial gradient minimum acceleration flows. We divide the quadrants in the matrices up into $\mathscr{T}$ coefficients (top left), $\mathscr{S}$ coefficients (bottom right), and $\mathscr{T}-\mathscr{S}$ covariant coefficients (top right and bottom left). We also calculate the trace for the $\mathscr{T}$ and $\mathscr{S}$ parts of the matrix. Twice as many poloidal flow coefficients are resolved as toroidal coefficients in all resolution matrices in Fig. 3. Our models derived from Swarm spatial gradients data resolve of around 1.4 times the number of flow coefficients as those derived from the vector data. The increase is less pronounced when comparing vector and spatial gradient flows from CHAMP, but still shows an improvement. This suggests that spatial gradient SV data from satellite measurements are beneficial for core-surface flow modelling.

Whereas resolution matrices show how well we resolve each flow-coefficient of our models, we can use averaging functions to evaluate the models' spatial resolution. Averaging functions describe how well localised a model estimate is at a given point in space. We calculate the averaging functions for the toroidal and poloidal flow potentials, $\mathscr{T}$ and $\mathscr{S}$, rather than the flows themselves. The averaging function, A, for a point on the CMB, (θ_0, ϕ_0), is given by:

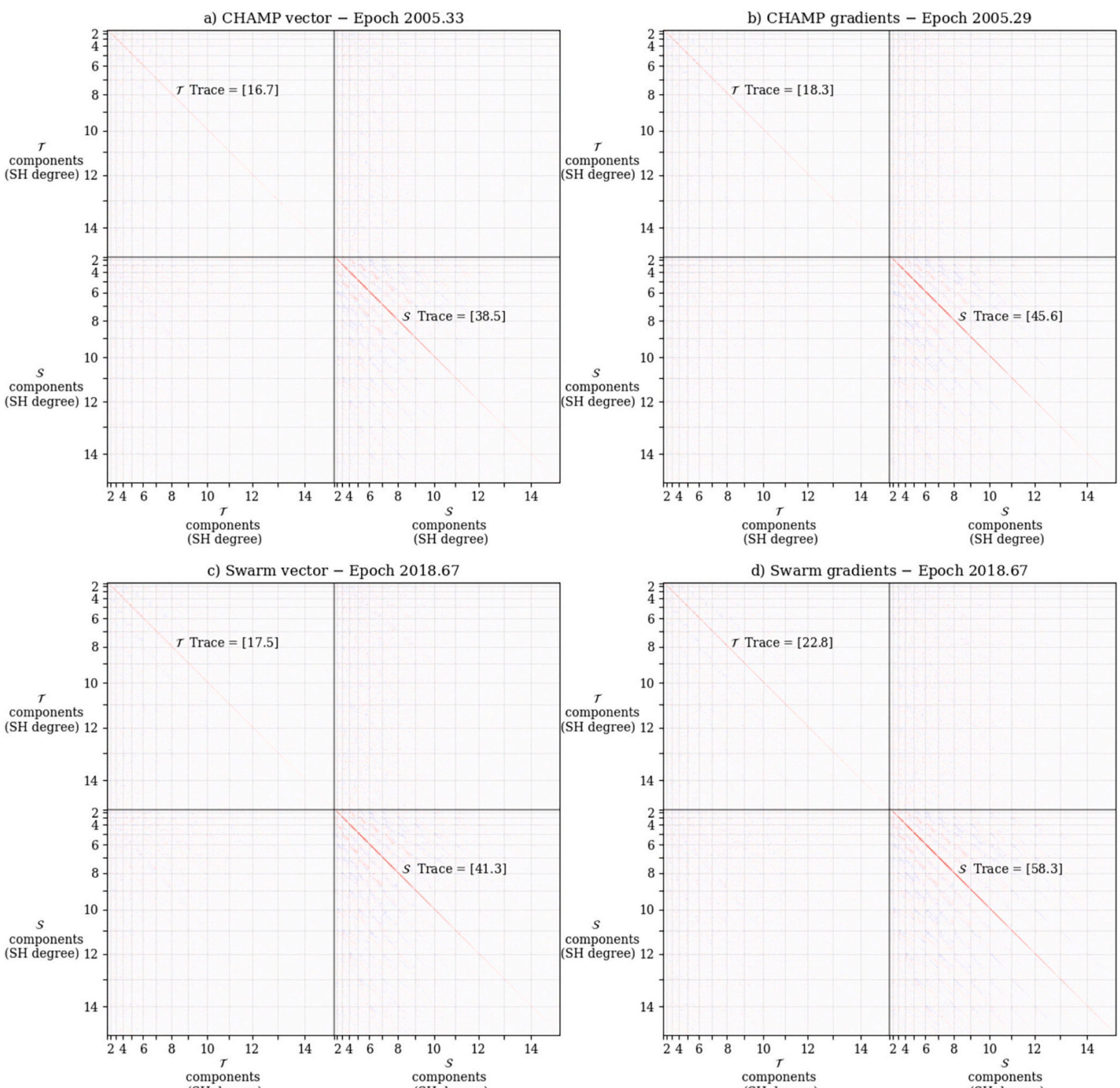

Fig. 3. Resolution matrices for minimum acceleration models using CHAMP (a, b) and Swarm (c, d) vector (a, c) and spatial gradients (b, d).

$$A(\theta_0, \phi_0, \theta, \phi) = \mathbf{c}^T(\theta_0, \phi_0)\mathbf{R}\mathbf{v}(\theta, \phi) \tag{12}$$

in which the vector $\mathbf{c}$ maps the location of (θ_0, ϕ_0) onto the vector $\mathbf{v}$, which contains the spherical harmonic representation of our model. They have elements of the form

$$P_n^m(\cos\theta_0)\left\{\begin{matrix}\cos m\phi_0 \\ \sin m\phi_0\end{matrix}\right\} \quad \text{and} \quad \frac{2n+1}{4\pi}\, P_n^m(\cos\theta)\left\{\begin{matrix}\cos m\phi \\ \sin m\phi\end{matrix}\right\}$$

respectively. The scalar A can thus be considered a physical-space version of the resolution matrix (see Appendix A for more detail on the averaging function). The perfect averaging function for an infinite spherical harmonic series is a double Dirac delta function centred at (θ_0, ϕ_0), i.e. it is perfectly localised at (θ_0, ϕ_0) encompassing an area of 1. However, for a truncated spherical harmonics series, the ideal averaging function will have a width inversely proportional to N, and side-lobes, which decrease as N_u increases (Whaler and Gubbins, 1981).

For $N_u = 14$, Whaler et al. (2016) found that the ideal A corresponds to an estimate over an area of at least an angle 30° subtended at the Earth's centre. An example of this is shown in Fig. 4a. We note here that the ideal averaging function will only be obtained for a model with an ideal resolution matrix, i.e., the identity matrix. For a regularised solution, achieving this will not be possible.

To get a global image of the spatial resolution, we plot in Fig. 5 the value of A, evaluated at the point at which it is centred, normalised by its maximum possible value of $\frac{56}{\pi}$ for our maximum spherical harmonic degree of $N_u = 14$, on a $1^\circ \times 1^\circ$ grid across the core-surface. We see from Fig. 5a and c that the poloidal flow potential, $\mathscr{S}$, appears well resolved at most locations, with normalised values reaching over 70% of the maximum possible value in regions under east Asia, the Indian Ocean, and the South Pacific for the gradient tensor-derived flow. However, we see a pronounced band of low values along the magnetic equator at the core surface, which extends into a region underneath the south Atlantic.

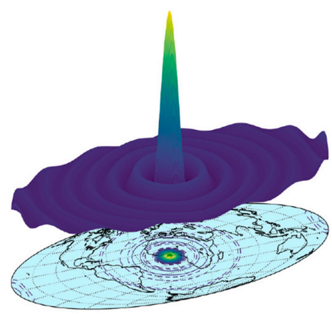

(a) Ideal averaging function for $N_u = 14$.

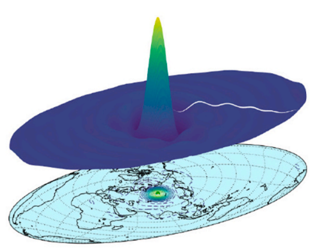

(b) Poloidal flow potential – centred at 59°N, 97°E

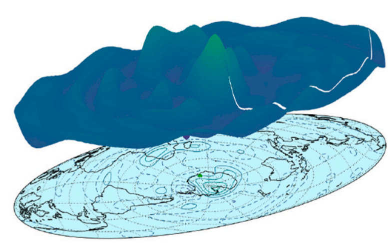

(c) Poloidal flow potential – centred at 73°S, 35°E

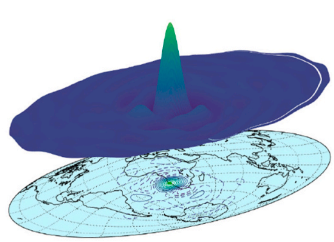

(d) Toroidal flow potential – centred at 21°S, 12°E

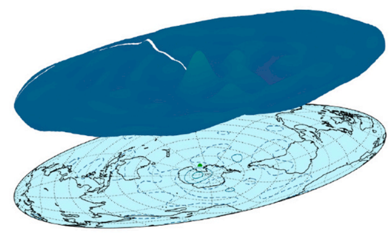

(e) Toroidal flow potential – centred at 75°S, 168°W

Fig. 4. Averaging functions for flow obtained from the Swarm spatial gradient tensor SV data. (a) shows the ideal averaging function for a flow with spherical harmonic degree $N_u = 14$, and has contour intervals of 1. (b, c) show the actual averaging functions for the poloidal flow potential, (d, e) show the actual averaging functions for the toroidal flow potential. (b, d) have contour intervals of 1, and (c, e) have contour intervals of 0.25. Negative contours are dashed, and continents are shown for reference.

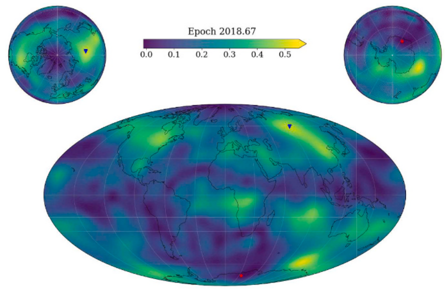

(a) Peak poloidal flow potential – Swarm vector data.

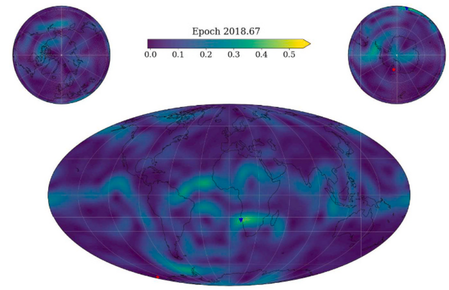

(b) Peak toroidal flow potential – Swarm vector data.

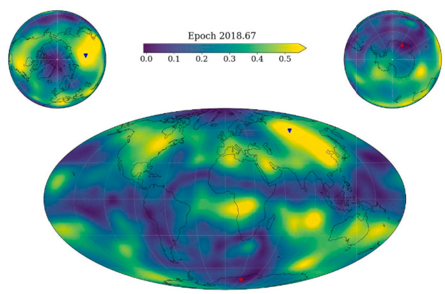

(c) Peak poloidal flow potential – Swarm gradient tensor data.

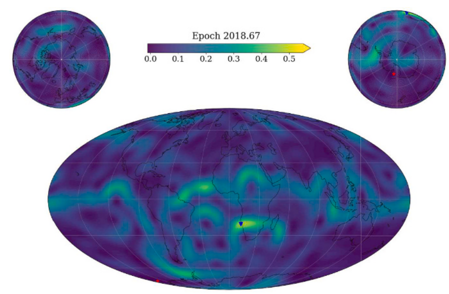

(d) Peak toroidal flow potential – Swarm gradient tensor data.

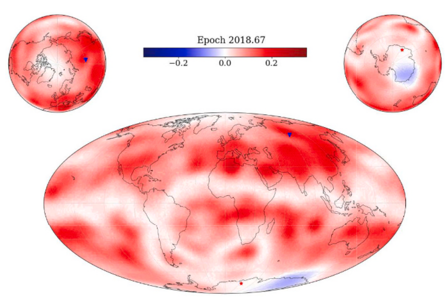

(e) Peak poloidal flow potential – Difference between Swarm gradient tensor and vector data values.

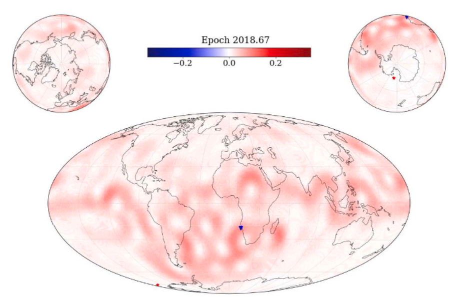

(f) Peak toroidal flow potential – Difference between Swarm gradient tensor and vector data values.

Fig. 5. Peak averaging functions at the point they are evaluated, normalised to the maximum possible value for $N = 14$ for flows using Swarm vector data (a, b), Swarm spatial gradient tensor (c, d), and their difference (e, f). (a, c, e) – Poloidal flow potential. (b, d, f) – Toroidal flow potential. Blue triangle and red star in (a, c, e) and (b, d, f) mark the maximum and minimum values in the peak averaging functions, respectively, and those averaging functions are shown in Fig. 4. (For interpretation of the references to colour in this figure legend, the reader is referred to the web version of this article.)

These low-value regions for averaging functions for $\mathscr{S}$ appear to be where those for $\mathscr{T}$ (Fig. 5b and d) are best resolved, despite having very low resolution almost everywhere else. Fig. 5e and f show the difference in the peak averaging function for spatial gradients and vector data, using our preferred values of damping parameters that give a roughly comparable misfit. For $\mathscr{S}$, the spatial resolution is greatly improved in all locations where we are able to resolve the flow (i.e. outside the aforementioned band of low values). For $\mathscr{T}$, we see an increase in resolution everywhere, particularly around the central Pacific. The few locations where the difference in peak averaging functions is negative are in locations where the resolution is already poor, possibly due to the non-unique nature of the problem at hand. We therefore interpret negative differences in peak average functions as locations where the gradients have constrained the parts of the flow we can resolve, thus sharpening the transition between resolved and unresolved regions. This confirms that using spatial gradients improves the flow resolution nearly everywhere.

In order to investigate the behaviour of the averaging functions, we evaluate them at the locations of maximum and minimum peak values from Fig. 5, as shown by the blue triangle and red star in Fig. 5c and d. At the maxima, shown in Fig. 4b and d, the averaging functions appear well-behaved and the peak is centred over the point at which it is evaluated. The averaging function for poloidal flow potential shows a larger peak and symmetric side lobes, compared to the toroidal flow potential, where the averaging function has a smaller maximum value, and weak azimuthal variation in the side lobes, but with a similar maximum height. For Fig. 4c and e, which show averaging functions at the minimum peak values in Fig. 5c and d, we see much lower values with no clear peak. Rather, Fig. 4c appears to have a small maximum offset from the central point. This suggests that the null-regions revealed by the peak averaging functions do not necessarily correspond to low amplitude averaging functions, but could also indicate averaging functions which are not centred at the point where they are evaluated. The toroidal potential averaging function at the minimum peak value (Fig. 4e) is almost flat, suggesting there is very little information about the toroidal flow in the area.

4.2. Investigating core-surface flow patterns

Based on the evidence presented in the previous section showing the improved spatial resolution using the spatial gradient tensor over the vector data, we henceforth concentrate on flows obtained using gradient data. We first compare the minimum acceleration and SA flows, to assess how much and where equatorial asymmetry is required. Fig. 6a shows a snapshot of the minimum acceleration flow in 2018.67. The minimum acceleration flows have familiar features commonly seen from vector data inversions, such as persistent westward drift at mid- to high latitudes and in the Atlantic region (e.g. Holme, 2015); eastward flow in the Pacific region (Ropp and Lesur, 2023); the presence of an eccentric planetary gyre (Pais and Jault, 2008); a westward polar jet with its associated daisy-chain SV pattern (Livermore et al., 2017; Gillet et al., 2019); and northwards cross-equatorial flow in the Western Pacific, close to the equator, with speeds up to 20 km yr^{-1} (Bloxham et al., 1989; Whaler et al., 2022; Ropp and Lesur, 2023). Therefore, we can use the minimum acceleration model as a baseline against which to compare the SA models. Any differences between those and the minimum acceleration models will be a direct consequence of limits to the amount of equatorially asymmetric flow permitted. Although not shown here, we note that snapshots of the minimum acceleration flows and TO-like flows exhibit similar flow patterns, as they have the same spatial damping.

The flow in Fig. 6a is superimposed on the poloidal potential, $\mathscr{S}$. Positive $\mathscr{S}$ values are indicative of divergent flow, whereas $\mathscr{S} < 0$ indicates convergent flow. We can therefore use these values as a proxy for up- and downwelling at the core-surface. Firstly, we note that there is an up-downwelling pair associated with the high-latitude Pacific jet. We also see a region of upwelling in the west equatorial Pacific, where the azimuthal flow direction changes from west to east, with a downwelling counterpart in the east equatorial Pacific. These regions of increased velocity potential were reversed and weaker in the CHAMP era (Supplementary Fig. B.3), during which the flow in the Pacific was much weaker, and was turning from westward to eastward (Ropp and Lesur, 2023).

Fig. 6b shows the SA flow for a snapshot during the Swarm period. We constructed this flow to be predominantly equatorially symmetric, as that is expected for a flow generating an axial dipole-like magnetic field. With this flow, we were able to provide an adequate data fit, without introducing any bias in the fit to individual GVOs. The flow is dominated by more smaller-scale features, which also shows in its resolution matrix, where the energy is less concentrated in the low-degree flow coefficients (Fig. B.2). The deviations from symmetry appear primarily in the high latitude jet and cross-equatorial flow beneath Indonesia, which are not mirrored across the equator. By comparing the minimum acceleration and SA flow, we can start to distinguish which features of the flow are persistent even after enforcing equatorial symmetry in the solution. For example, the toroidal flow in the Indian Ocean only appears in the Southern hemisphere in the minimum acceleration flows, but is mirrored to appear both in the Northern and Southern hemisphere in the SA flows. That this feature in the Southern hemisphere is required to obtain an acceptable fit to the data, as seen by the data predictions at a nearby GVO in Fig. 2, suggests that it is a robust feature of the core-surface flow.

4.3. Investigating temporal behaviour

Having looked at the structure of the flow, we investigate modelled flow behaviour over time. The rms velocity, and percentage spatial statistics of the flows (from vector data only) are given in Fig. 7 for both CHAMP and Swarm as a function of time. The flows have an rms velocity of around 11 km yr^{-1}, and are predominantly toroidal, equatorially symmetric, and geostrophic, with about 15% deviation from these descriptors. Comparing the flows between CHAMP and Swarm eras, the poloidal flow is stronger during the CHAMP era. These features have also been observed by Ropp and Lesur (2023) using different methodologies and datasets, pointing to them being a feature of the core-flow, rather than model-specific differences. The increase in proportional poloidal flow could be a manifestation of the west-east Pacific up-downwelling pairs (noted in Section 4.2). The strongest difference between our CHAMP and Swarm era flows is the proportional energy in the zonal toroidal flow components, which is almost twice as high in the CHAMP compared to the Swarm eras. We found that this difference arises from the deviation from westward flow under the equatorial Pacific during the Swarm era, thus reducing the proportional amount of zonal toroidal flow, usually considered to describe westward drift (Suttie et al., 2025).

4.4. Comparing flow models to ΔLOD predictions

It is possible to relate core-surface flow to ΔLOD, based on the

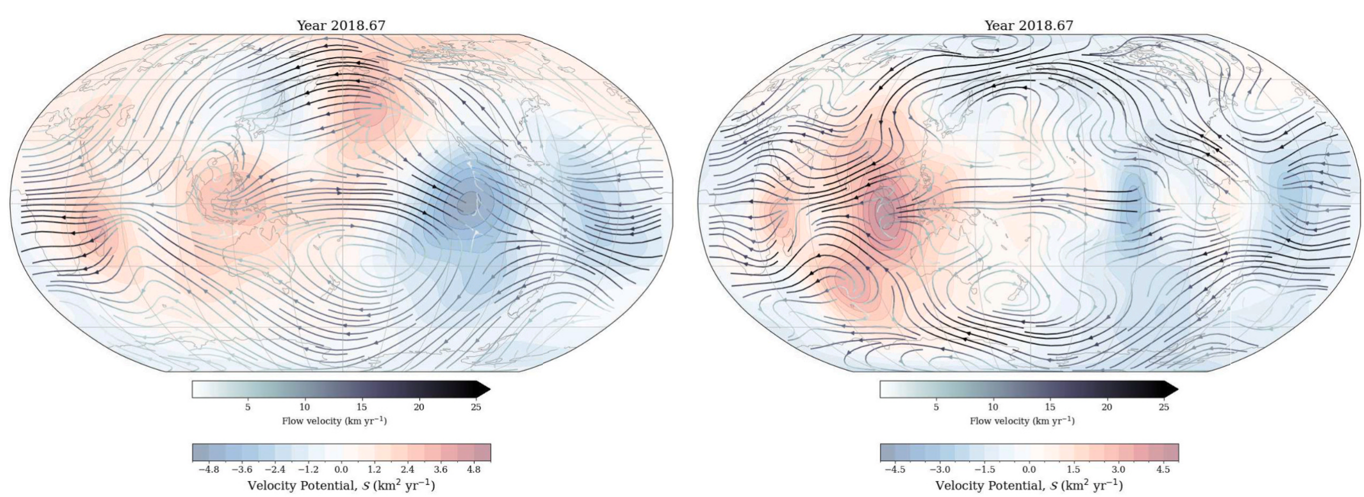

(a) Minimum acceleration (b) SA

Fig. 6. Flow snapshot in 2018.67 from Swarm spatial gradient data, superimposed on the poloidal velocity potential, $\mathscr{S}$, which is associated with up- ($\mathscr{S} > 0$) and downwelling ($\mathscr{S} < 0$). a) Minimum acceleration and b) SA flow model. Difference in flow strength is caused by difference in damping between models to achieve a similar misfit. Plot is centred at 180° longitude in Mollweide projection. Continents are shown for reference only.

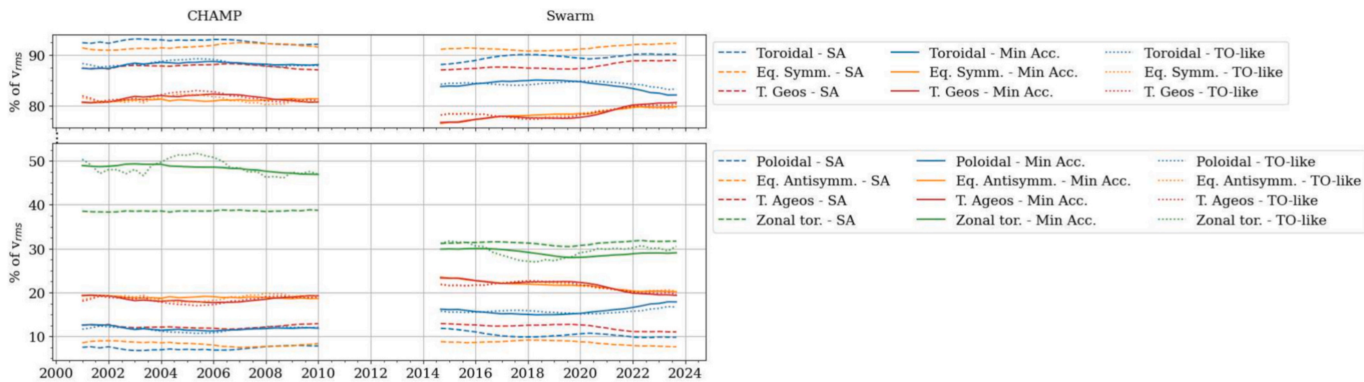

Fig. 7. Temporal variation of the percentage spatial statistics of flows from CHAMP and Swarm vector data for the minimum acceleration model (solid line), SA model (dashed line), and TO-like model (dotted line). Note that top and bottom panel show different ranges of the same quantity. Note also that each colour represents a different part of the flow, unlike other figures where each colour represents a different flow model. Abbreviations: Min. Acc. – Minimum acceleration; Eq. Symm. – Equatorially symmetric; T. Geos – Tangentially geostrophic; Eq. Antisymm. – Equatorially antisymmetric; T. Ageos – Tangentially ageostrophic; Zonal tor. – Zonal toroidal.

relation originally given by Jault et al. (1988), and updated by Jault and Finlay (2015) to

$$\Delta \text{LOD} = 1.232\left(t_1^0 + 1.776t_3^0 + 0.080t_5^0 + 0.002t_7^0\right), \tag{13}$$

where t_n^0 are zonal toroidal velocity coefficients of the n^{th} degree. Using this relation, we show the flow-predicted ΔLOD from the CHAMP and Swarm eras using the three types of flow models in Fig. 8 together with the observed values. Firstly, we see that predictions of the minimum acceleration and SA flows are very similar using both vector and spatial gradient data, and tend to under-predict the ΔLOD changes. During the CHAMP period, these models predict virtually no changes, compared to observed values which increase after 2004. For Swarm to date, the models accurately predict the fall and rise in ΔLOD, but show a sharper increase than the observed ΔLOD after 2020. For the TO-like models, we see much more variation in amplitude in predicted ΔLOD. For CHAMP, the predictions are very scattered, but consistent with the increase in ΔLOD in 2005. For the Swarm period, the TO-like models show a good fit to the data from 2018 and onwards, but while the observed ΔLOD remains fairly constant around 1.0 ms from 2014 to 2017, the Swarm model predictions show a steep increase from −0.5 ms to 1.0 ms in this period. Comparing TO-like models based on spatial gradients and vector data, the predicted ΔLOD from spatial gradient-based models is much smoother than when using vector data only.

4.5. *Azimuthal flow acceleration - a new jerk in 2024?*

During the CHAMP era, three clear jerks in the equatorial Atlantic were observed - in 2003.5, 2007, and 2011 (e.g. Brown et al., 2013; Chulliat and Maus, 2014). Chulliat and Maus (2014) suggested that they were the result of a standing wave in secular acceleration with a period of around 6 years. In the Swarm era, two jerks have been observed in the

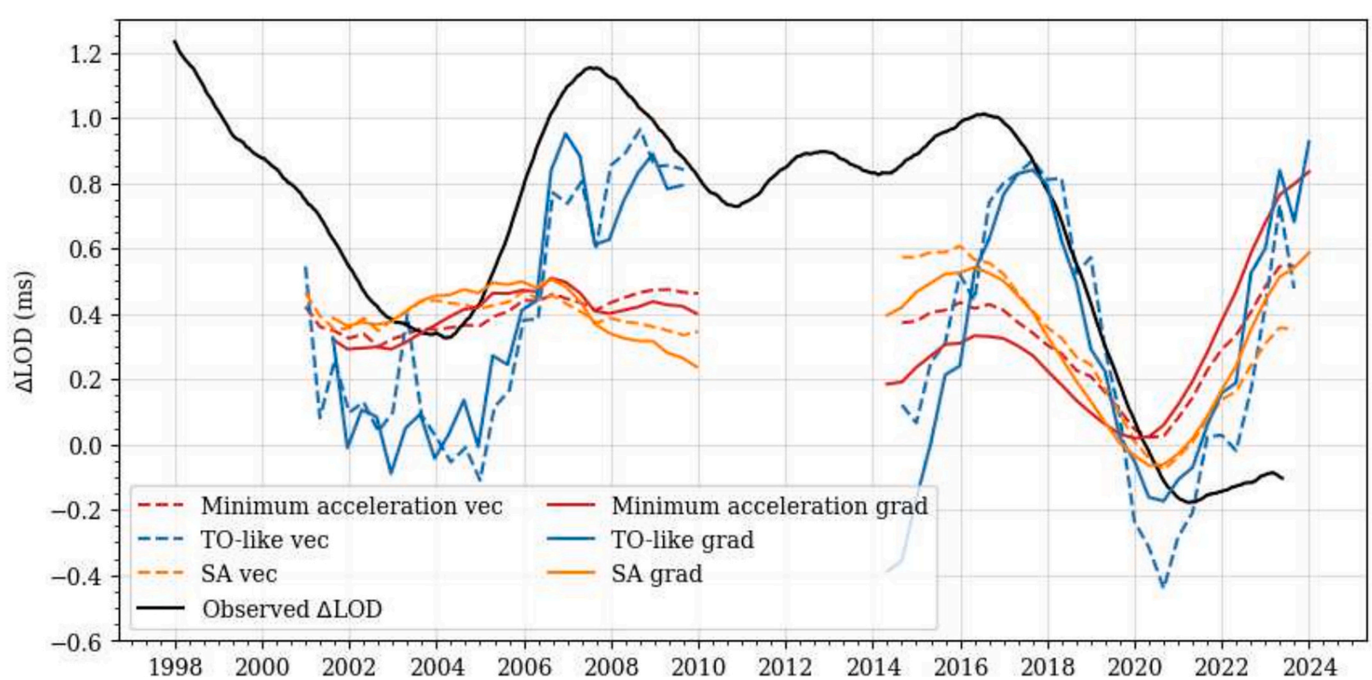

Fig. 8. Flow-predicted ΔLOD from CHAMP (2001–2010) and Swarm (2014–2024) from the minimum acceleration flows (red), SA flows (orange), and TO-like flows, using spatial gradients (solid lines) and vector (dashed lines) data. Black curve shows atmospherically and tidally corrected ΔLOD observations with an annual running mean (Madsen and Holme, in review). The flow-predicted ΔLOD time series have an arbitrary offset in the y-axis for clarity. (For interpretation of the references to colour in this figure legend, the reader is referred to the web version of this article.)

equatorial Pacific - one in 2017 (e.g. Finlay et al., 2020) and another in 2020 (Campuzano et al., 2021). Whaler et al. (2022) noted that the 2017 jerk is associated with a sudden change in azimuthal core-surface flow acceleration, a_ϕ. We follow their approach, and look at the core-surface flow acceleration associated with these jerks.

We obtain flow acceleration from finite first differences of our core-surface flows at each epoch, with a time-step of 4-months. Fig. 9 shows a snapshot of the azimuthal acceleration in 2018.67 – the temporal midpoint between the 2017 and 2020 Pacific jerks. We see that the values of a_ϕ are generally below 2 km yr^{-2} globally. The greatest deviations from this are in the region beneath the west equatorial Pacific, where we see a strong peak in eastward a_ϕ of over 5 km yr^{-2}, centred around 175°W, and a smaller peak around 130°W, both north of the equator. The temporal evolution of these localised peaks is shown in the time-latitude plots in Fig. 9b. The peaks are associated with a pulse-like feature, centred beneath the west Pacific. The pulses peak around 2018.67, and cross zero azimuthal acceleration in 2017 and 2020, concurrent with the geomagnetic jerks observed in these regions. Interestingly, we see a second pulse with a negative peak in 2022.00 in the same region at both locations, now with westward acceleration, and a peak of around −4 km yr^{-2}. Continuing at the rate indicated, the acceleration amplitude would reach zero in the year 2024, which suggests a possible geomagnetic jerk in this region then. Given that geomagnetic jerks are defined as inflections in SV, and SV is obtained from annual differences in magnetic field measurements, the soonest it would be possible to confirm this would be in early 2025.

5. Discussion

In this study, we compare the results of flow-inversions using GVO SV vector and spatial gradient data. We show that using spatial gradient data yields a lower overall model rms misfit to the data. From analysing the resolution of the resulting flow models, we also find that models based on spatial gradient data resolve more flow coefficients, both

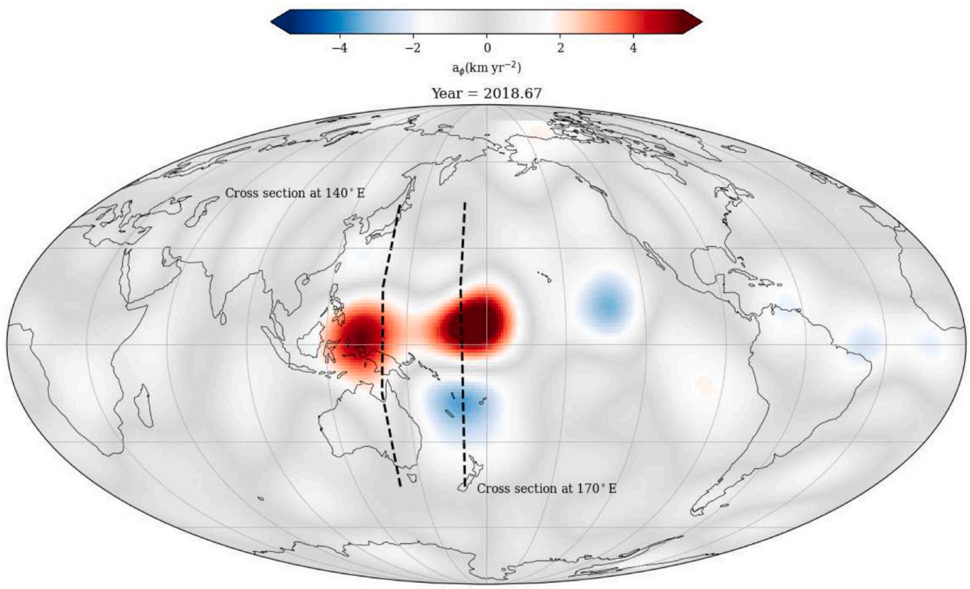

(a) Global a_ϕ snapshot in 2018.67.

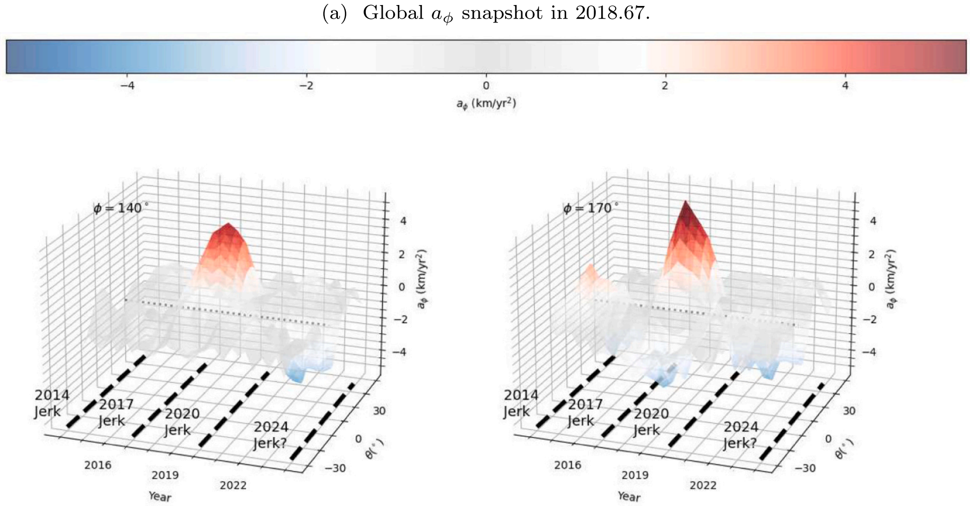

(b) Time-latitude plot for constant longitude 140°W and 170°W

Fig. 9. Azimuthal flow acceleration, a_ϕ, from the minimum acceleration flow model obtained from Swarm spatial gradient SV data. $a_\phi > 0$ signifies eastward acceleration, and $a_\phi < 0$ signifies westward acceleration. Values of $|a_\phi| < 1.8$ km yr^{-2} are in grey to highlight acceleration pulses. Note that the colour scale is clipped at ±5 km yr^{-2}. a) Global a_ϕ snapshot in 2018.67, centred at 180° longitude in Mollweide projection. Continents are shown for reference only. b) Time-latitude plots of a_ϕ, covering ±30° latitude at constant longitudes.

toroidal and poloidal, and improve the spatial resolution of the flow (see Fig. 5e and f). We note that resulting resolution matrices for a given inversion are directly influenced by the choice of damping parameters, as follows from Eq. (11). Even for CHAMP, where the spatial gradient-based model was more heavily spatially damped than the vector-based model (Table B.3), we find an increased trace value for both poloidal and toroidal flow coefficients. Similarly, when looking at the difference in averaging functions in Fig. 5e and f, we see that using spatial gradient data improves the spatial resolution nearly everywhere across the core surface. The only exception in Fig. 5e is where the spatial gradients yield poorer resolution for poloidal flow beneath the east Antarctic. However, the decrease in resolution occurs around an ambiguous band where the poloidal flow potential is ill-determined from both the vector and spatial gradient data. This low in the peak poloidal averaging functions overlaps with a maximum in peak toroidal averaging functions, and appears to follow the magnetic equator at the CMB, with a spiral around the south Atlantic, verging towards Antarctica at 0° longitude. We suggest that the region where the difference in peak averaging functions between vector and spatial gradient-based flows is negative is a result of the spatial gradients better capturing the boundary between the areas in which we can resolve the poloidal flow and those where we cannot. This likely highlights a localised ambiguous region rather than a region of poorer resolution. We suggest further investigation of averaging functions for core-surface flow modelling is required, particularly with satellite era SV datasets which offer complete spatial coverage. The localised ambiguous region seen in the averaging functions was found by Whaler et al. (2016), but they were influenced by the unequal data-distribution associated with ground observatories; we find the same structure from using homogeneously distributed GVO data, validating their result.

Our minimum acceleration flows are predominantly toroidal, equatorially symmetric, and tangentially geostrophic, as shown in Fig. 7, and contain features in flows seen in numerous other studies; the planetary gyre (e.g. Pais and Jault, 2008), high-latitude jet (Livermore et al., 2017), and eastward equatorial flow in the Pacific (Ropp and Lesur, 2023). It is reassuring that these features appear when relying only on geomagnetic data, without the use of geodynamo priors, suggesting that they are indeed present in the core. From the poloidal flow potential, superimposed on the total flow in Fig. 6, it appears that the eastward flow in the Pacific, and the acceleration of the high-latitude jet, are dominated by up- and downwelling pairs. This is contrary to the traditional view of the global flow, that usually describes global westward flow and “the quiet Pacific” (e.g. Gubbins and Roberts, 1987; Holme, 2015). This possibly reflects the lack of information over the Pacific in pre-satellite eras, due to the distribution of ground observatories. Further analysis of a continuous flow model covering a longer period (e.g. that of Ropp and Lesur, 2023, or Grüne et al. (in review for this issue)), could illuminate the dynamics of this change.

Given the ill-determined nature of core-flow modelling, obtaining a unique flow from the induction equation requires further assumptions. Some physical assumptions frequently imposed are that the flow is tangentially geostrophic (Le Mouël, 1984), columnar (Amit and Olson, 2004), or quasi-geostrophic (Pais and Jault, 2008; Gillet et al., 2009). In the example of tangentially geostrophic flows and columnar flows, equatorial symmetry is implied, and is often enforced when using the quasi-geostrophic assumption (e.g. Gillet et al., 2009; Amit and Pais, 2013). In Section 4.2, we discuss the features of the flow that appear when we penalise equatorial asymmetry, such as the cross equatorial flow under Indonesia. We found that at least 10% of the flow energy must be equatorially asymmetric in order to fit the Swarm data. Forcing equatorial symmetry could thus result in a misrepresentation of the core-surface flow. Assumptions which rely on equatorial symmetry (either implicitly or explicitly) capture the first-order features of the field that are known to be important in geodynamo mechanisms (e.g. Aubert and Gillet, 2021), but the higher quality of recent data means we must include equatorial asymmetry to model the data properly. We therefore recommend using nonuniqueness-reducing norms independent of flow geometry, such as the strong norm (Bloxham, 1988) used here, minimising the kinetic energy of the flow (Whaler, 1986; Beggan and Whaler, 2008), or even minimising the amount of radial core SV generated by advection (e.g. Whaler, 1986).

In Section 4.4, we compared the predictions of ΔLOD from each of our models to observations. Our calculation – and indeed the one adopted most frequently with various degrees of success (e.g. Wardinski et al., 2008; Gillet et al., 2010; Whaler et al., 2016; Bärenzung et al., 2018; Istas et al., 2023; Rosat and Gillet, 2023) – relies on the assumption that the only contributing core-surface flow components to ΔLOD changes are geostrophic (Jault et al., 1988; Jault and Finlay, 2015). A recent synthetic study by Schwaiger et al. (2024) found that the quasi-geostrophic assumption was valid for 90% of the core-surface flow from the 71p geodynamo model (Aubert and Gillet, 2021), although they do note that this is not an accurate representation of the real Earth. By comparing the ΔLOD calculated from their inverted flow and the observed flow to the ΔLOD result from the dynamo simulation, they find an overall good fit, with periods of deviation between the result from the inverted and observed core-surface flow. This suggests either that the non-geostrophic flow components, or the small scale flow-components that are inaccessible from flow-inversions, are required to predict ΔLOD satisfactorily. This offers a possible explanation as to why the predicted ΔLOD from core-surface flow obtained by inversion only occassionally fits observations.

Recently, numerical dynamo simulations have offered an explanation for the underlying dynamics that govern geomagnetic jerks. Aubert et al. (2022) argue that the majority of the jerks in their simulations occur when there are local disruptions to the leading-order force balance, causing quasi-geostrophic Alfvén waves to emerge where the force balance is disturbed. As these waves interact with the flow at the core-surface, geomagnetic jerks occur. If this is true, our study provides evidence of these waves arriving at the core-surface with the CHAMP- (Fig. B.4) and Swarm-era (Fig. 9) flows, without relying on spectral methods or data assimilation. Reminiscent of the study of Chulliat et al. (2010), our results show that the 2017 and 2020 geomagnetic jerks in the Pacific can both be explained by a pulse in azimuthal flow acceleration. (We also suggest a similar explanation for the 2003.5 and 2007 jerks from the flows obtained from CHAMP spatial gradient data, as shown in Fig. B.4.) Chulliat and Maus (2014) related the cascade of equatorial geomagnetic jerks in the Atlantic to a standing wave with a period of about 6 years, which they suggest is an equatorial magneto-Coriolis wave. The pulses we obtain in azimuthal acceleration appear to have the same periodicity of around 6–7 years, similar to the magneto-Coriolis modes found by Gerick and Livermore (2024).

Finally, we note that if this mechanism for equatorial geomagnetic jerks is correct, it offers a short-term prediction method for forecasting them. As shown by Chulliat and Maus (2014) for secular acceleration, and here for azimuthal flow acceleration, equatorial geomagnetic jerks appear to be associated with a change of sign of these acceleration pulses. Currently, it is impossible to predict the spatiotemporal onset of such a pulse as the proposed wave arrives at the core surface. However, its collapse is associated with a geomagnetic jerk around the location of the pulse when the acceleration changes sign. Given that these pulses tend to have a period of 6–7 years, once an equatorial geomagnetic jerk appears in a new region, we can expect to see a counterpart 3–3.5 years later. The implications of this could be useful for geomagnetic forecasting, for example for the International Geomagnetic Reference Field (e.g. Fournier et al., 2021).

6. Conclusion

We invert four-monthly mean GVO spatial gradient SV tensor and vector data from the CHAMP and Swarm satellites to produce global flow models. We found that using spatial gradients significantly improved the spatial resolution of the flows. We created three flows, all regularised to minimise acceleration and spatial complexity; minimum acceleration, SA, and TO-like flows. We found the minimum amount of equatorial antisymmetry required to fit the data is about 10% for Swarm data. By relaxing the temporal damping on the odd zonal toroidal coefficients, we find flows that are better able to fit observations in ΔLOD. All three models resolve the 2017 and 2020 geomagnetic jerks, which are associated with pulses in low latitude azimuthal acceleration with a period of 6–7 years. These are consistent with the arrival of Alfvén waves from the deeper outer core, as proposed by Aubert et al. (2022). Following this assumption, we forecast a jerk in the western Pacific Ocean in late 2024.

CRediT authorship contribution statement

Frederik Dahl Madsen: Conceptualization, Methodology, Formal analysis, Investigation, Software, Writing – original draft, Writing – review & editing, Visualization. **Kathryn A. Whaler:** Conceptualization, Methodology, Software, Writing – original draft, Writing – review & editing, Supervision. **Ciarán D. Beggan:** Conceptualization, Methodology, Writing – original draft, Writing – review & editing, Supervision. **William J. Brown:** Conceptualization, Methodology, Writing – original draft, Writing – review & editing, Supervision. **Jonas Bregnhøj Lauridsen:** Data curation. **Richard Holme:** Conceptualization, Supervision.

Declaration of competing interest

The authors declare that they have no known competing financial interests or personal relationships that could have appeared to influence the work reported in this paper.

Acknowledgements

We are grateful to the editorial team for this special issue, and for the encouragement to contribute. We are also grateful to the Prof. Philip W Livermore, and one anonymous reviewer, for useful comments that improved this manuscript. We thank Nils Olsen for discussions on averaging functions, and Naomi Shakespeare-Rees for discussions on up- and downwelling. FDM was supported by a NERC Doctoral Training Partnership grant (NE/S007407/1) and in part funded by BGS University Funding Initiative PhD studentship S493. KAW was supported partly by ESA through the Swarm DISC activities, funded by ESA contract no. 4000109587.

Appendix A. Averaging functions for scalar potentials

Here, we provide more information regarding the averaging functions for scalar flow potentials. We follow the derivation of Whaler and Gubbins (1981) for averaging functions for the vertical magnetic field component at the CMB, but here applied to the toroidal scalar $\mathscr{T}$ (that for $\mathscr{S}$ follows similarly). Numbers in parentheses refer to the equivalent equation in Whaler and Gubbins (1981).

Using the orthogonality of Schmidt quasi-normalised spherical harmonics, from Eq. (5) we have (4.2)

$$t_n^{m\,c} = \frac{2n+1}{4\pi}\oint_{\Omega} \mathscr{T}(\theta,\phi)\, P_n^m(\cos\theta)\, \cos m\phi \,\mathrm{d}\Omega \tag{A.1}$$

where Ω is the CMB, and similarly for $t_n^{m\,s}$.

We then write our estimate of $\mathscr{T}$ at a point on the CMB, (θ_0,ϕ_0), $\overline{\mathscr{T}}$, as (4.3)

$$\overline{\mathscr{T}}(\theta_0,\phi_0) = \sum_{n=1}^{N_u}\sum_{m=0}^{n}\left(\alpha_n^m(\theta_0,\phi_0)\, t_n^{m\,c}(\theta,\phi) + \beta_n^m(\theta_0,\phi_0)\, t_n^{m\,s}(\theta,\phi)\right) = \oint_{\Omega} A(\theta,\phi,\theta_0,\phi_0)\,\mathscr{T}(\theta,\phi)\,\mathrm{d}\Omega \tag{A.2}$$

where

$$A(\theta,\phi,\theta_0,\phi_0) = \sum_{n=1}^{N_u}\sum_{m=0}^{n}\frac{(2n+1)}{4\pi}P_n^m(\cos\theta)\left(\alpha_n^m(\theta_0,\phi_0)\cos m\phi + \beta_n^m(\theta_0,\phi_0)\sin m\phi\right), \tag{A.3}$$

and α_n^m and β_n^m are the spherical harmonic weighting coefficients of the averaging functions.

We can then write the weighting coefficients as (4.6)

$$\alpha_n^m(\theta_0,\phi_0) = P_n^m(\cos\theta_0)\cos m\phi_0 \tag{A.4}$$

and similarly for $\beta_n^m(\theta_0,\phi_0)$. Hence

$$A(\theta,\phi,\theta_0,\phi_0) = \sum_{n=1}^{N_u}\sum_{m=0}^{n}\frac{2n+1}{4\pi}P_n^m(\cos\theta)P_n^m(\cos\theta_0)(\cos m\phi_0\cos m\phi + \sin m\phi_0 \sin m\phi) \tag{A.5}$$

Utilising the addition theorem for spherical harmonics (we refer the reader to Eqs. (3.4)–(3.6) of Winch et al., 2005, presented for Schmidt quasi-normalised spherical harmonics), this expression reduces to (4.7)

$$A(\psi) = \sum_{n=1}^{N_u}\frac{2n+1}{4\pi}P_n(\cos\psi), \tag{A.6}$$

where ψ is the angle subtended between (θ_0,ϕ_0) and (θ,ϕ), thus showing that as $N_u\rightarrow\infty$, the averaging function converges to a double Dirac delta function centred at (θ_0,ϕ_0).

We can rewrite Eq. (A.5) as

$$A(\theta,\phi,\theta_0,\phi_0) = \mathbf{c}^T(\theta_0,\phi_0)\mathbf{v}(\theta,\phi) \tag{A.7}$$

where **c** consists of the ordered $\alpha_n^m(\theta_0,\phi_0)$ and $\beta_n^m(\theta_0,\phi_0)$ and **v** has elements $\frac{2n+1}{4\pi}P_n^m(\cos\theta)\left\{\begin{array}{c}\cos m\phi\\ \sin m\phi\end{array}\right\}$ for each degree and order, n and m, respectively. Whaler and Gubbins (1981) Eq. (4.10) gives an example of how the α_n^m for the vertical magnetic field component at the CMB are modified by regularisation. From this, the (more general) averaging function, as presented by Bloxham et al. (1989) and in Eq. (12), can be written as

$$A(\theta_0,\phi_0,\theta,\phi)=\mathbf{c}^T(\theta_0,\phi_0)\mathbf{R}\mathbf{v}(\theta,\phi) \tag{A.8}$$

where **R** is the resolution matrix. If our potential is resolved perfectly, and hence $\mathbf{R}=\mathbf{I}$, where **I** is the identity matrix, then we recover the averaging function given by Eq. (A.5). However, as **R** deviates from the identity matrix, **R** skews the averaging function, thus showing how we can treat A as a physical-space version of **R**.

Appendix B. Supplementary data

Supplementary data to this article can be found online at https://doi.org/10.1016/j.pepi.2025.107336.

Data availability

CHAMP vector GVOs are available on the DTU's website; `https://www.space.dtu.dk/english/research-divisions/geomagnetism-and-geospace/projects/geomagnetic-virtual-observatories`. Swarm vector GVOs are available from the Swarm Data, Innovation, and Science Cluster (DISC); `https://swarm-diss.eo.esa.int/`. All CHAOS-7 models are available from; `https://www.spacecenter.dk/files/magnetic-models/CHAOS-7/`. Tidally cleaned ΔLOD data are available from the Earth Observation Centre; `https://hpiers.obspm.fr/eop-pc/index.php`.

References

Amit, H., Olson, P., 2004. Helical core flow from geomagnetic secular variation. Phys. Earth Planet. In. 147, 1–25. https://doi.org/10.1016/J.PEPI.2004.02.006.

Amit, H., Pais, M.A., 2013. Differences between tangential geostrophy and columnar flow. Geophys. J. Int. 194, 145–157. https://doi.org/10.1093/gji/ggt077.

Aubert, J., Finlay, C.C., 2019. Geomagnetic jerks and rapid hydromagnetic waves focusing at Earth's core surface. Nat. Geosci. 12, 393–398. https://doi.org/10.1038/s41561-019-0355-1.

Aubert, J., Gillet, N., 2021. The interplay of fast waves and slow convection in geodynamo simulations nearing Earth's core conditions. Geophys. J. Int. 225, 1854–1873. https://doi.org/10.1093/gji/ggab054.

Aubert, J., Livermore, P.W., Finlay, C.C., Fournier, A., Gillet, N., 2022. A taxonomy of simulated geomagnetic jerks. Geophys. J. Int. 231, 650–672. https://doi.org/10.1093/gji/ggac212.

Backus, G.E., 1983. Application of mantle filter theory to the magnetic jerk of 1969. Geophys. J. Int. 74, 713–746. https://doi.org/10.1111/j.1365-246X.1983.tb01901.x.

Bärenzung, J., Holschneider, M., Wicht, J., Sanchez, S., Lesur, V., 2018. Modeling and predicting the short-term evolution of the geomagnetic field. J. Geophys. Res. Solid Earth 123, 4539–4560. https://doi.org/10.1029/2017JB015115.

Beggan, C., Whaler, K., 2008. Core flow modelling assumptions. Phys. Earth Planet. In. 167, 217–222. https://doi.org/10.1016/J.PEPI.2008.04.011.

Beggan, C.D., Whaler, K.A., 2009. Forecasting change of the magnetic field using core surface flows and ensemble Kalman filtering. Geophys. Res. Lett. 36. https://doi.org/10.1029/2009GL039927.

Bloxham, J., 1988. The determination of fluid flow at the core surface from geomagnetic observations. In: Vlaar, N.J., Nolet, G., Wortel, M.J.R., Cloetingh, S.A.P.L. (Eds.), Mathematical Geophysics: A Survey of Recent Developments in Seismology and Geodynamics. Springer, Netherlands, Dordrecht, pp. 189–208. https://doi.org/10.1007/978-94-009-2857-2_9.

Bloxham, J., Gubbins, D., Jackson, A., 1989. Geomagnetic secular variation. Philos. Trans. R. Soc. London, Ser. A 329, 415–502. https://doi.org/10.1098/rsta.1989.0087.

Bloxham, J., Zatman, S., Dumberry, M., 2002. The origin of geomagnetic jerks. Nature 420, 65–68. https://doi.org/10.1038/nature01134.

Brown, W.J., Mound, J.E., Livermore, P.W., 2013. Jerks abound: an analysis of geomagnetic observatory data from 1957 to 2008. Phys. Earth Planet. In. 223, 62–76. https://doi.org/10.1016/J.PEPI.2013.06.001.

Cain, J.C., Wang, Z., Schmitz, D.R., Meyer, J., 1989. The geomagnetic spectrum for 1980 and core-crustal separation. Geophys. J. Int. 97, 443–447. https://doi.org/10.1111/j.1365-246X.1989.tb00514.x.

Campuzano, S.A., Pavón-Carrasco, F.J., De Santis, A., González-López, A., Qamili, E., 2021. South Atlantic anomaly areal extent as a possible Indicator of geomagnetic jerks in the satellite era. Front. Earth Sci. 8. https://doi.org/10.3389/feart.2020.607049.

Chulliat, A., Maus, S., 2014. Geomagnetic secular acceleration, jerks, and a localized standing wave at the core surface from 2000 to 2010. J. Geophys. Res. Solid Earth 119, 1531–1543. https://doi.org/10.1002/2013JB010604.

Chulliat, A., Thébault, E., Hulot, G., 2010. Core field acceleration pulse as a common cause of the 2003 and 2007 geomagnetic jerks. Geophys. Res. Lett. 37. https://doi.org/10.1029/2009GL042019.

Courtillot, V., Ducruix, J., Le Mouël, J.L., 1978. Recent acceleration in the secular variation of the Earth's magnetic field. Comptes Rendus Hebdomadaires des Seances de l'Academie des Sciences Serie D 287, 1095–1098.

Duan, P., Huang, C., 2020. Intradecadal variations in length of day and their correspondence with geomagnetic jerks. Nat. Commun. 11, 2273. https://doi.org/10.1038/s41467-020-16109-8.

Eymin, C., Hulot, G., 2005. On core surface flows inferred from satellite magnetic data. Phys. Earth Planet. In. 152, 200–220. URL: https://www.sciencedirect.com/science/article/pii/S0031920105001214 https://doi.org/10.1016/j.pepi.2005.06.009.

Finlay, C.C., Jackson, A., 2003. Equatorially dominated magnetic field change at the surface of Earth's Core. Science 300, 2084–2086. https://doi.org/10.1126/science.1083324.

Finlay, C.C., Kloss, C., Olsen, N., Hammer, M.D., Tøffner-Clausen, L., Grayver, A., Kuvshinov, A., 2020. The CHAOS-7 geomagnetic field model and observed changes in the South Atlantic anomaly. Earth Planets Space 72, 156. https://doi.org/10.1186/s40623-020-01252-9.

Fournier, A., Aubert, J., Lesur, V., Thébault, E., 2021. Physics-based secular variation candidate models for the IGRF. Earth Planets Space 73, 190. https://doi.org/10.1186/s40623-021-01507-z.

Friis-Christensen, E., Lühr, H., Hulot, G., 2006. Swarm: a constellation to study the Earth's magnetic field. Earth Planets Space 58, 351–358. https://doi.org/10.1186/BF03351933.

Gerick, F., Livermore, P.W., 2024. Interannual Magneto–Coriolis modes and their sensitivity on the magnetic field within the Earth's core. In: Proceedings of the Royal Society A: Mathematical, Physical and Engineering Sciences, 480. https://doi.org/10.1098/rspa.2024.0184.

Gibson, R.D., Roberts, P.H., 1969. The Bullard-Gellman dynamo. In: Runcorn, S.K. (Ed.), Applications of Modern Physics to the Earth and Planetary Interiors, pp. 577–602.

Gillet, N., Pais, M.A., Jault, D., 2009. Ensemble inversion of time-dependent core flow models. Geochem. Geophys. Geosyst. 10. https://doi.org/10.1029/2008GC002290.

Gillet, N., Jault, D., Canet, E., Fournier, A., 2010. Fast torsional waves and strong magnetic field within the Earth's core. Nature 465, 74–77. https://doi.org/10.1038/nature09010.

Gillet, N., Jault, D., Finlay, C.C., 2015. Planetary gyre, time-dependent eddies, torsional waves, and equatorial jets at the Earth's core surface. J. Geophys. Res. Solid Earth 120, 3991–4013. https://doi.org/10.1002/2014JB011786.

Gillet, N., Huder, L., Aubert, J., 2019. A reduced stochastic model of core surface dynamics based on geodynamo simulations. Geophys. J. Int. 219, 522–539. https://doi.org/10.1093/gji/ggz313.

Gillet, N., Gerick, F., Jault, D., Schwaiger, T., Aubert, J., Istas, M., 2022. Satellite magnetic data reveal interannual waves in Earth's core. Proc. Natl. Acad. Sci. 119, e2115258119. https://doi.org/10.1073/pnas.2115258119.

Gillet, N., Dall'Asta, F., Amblard, P.O., Claveau, R., Aubert, J., 2024. Waves in Earth's core and geomagnetic field forecast. Phys. Earth Planet. In. 357, 107284. URL: https://www.sciencedirect.com/science/article/pii/S0031920124001420 https://doi.org/10.1016/j.pepi.2024.107284.

Gubbins, D., Roberts, P.H., 1987. Magnetohydrodynamics of the Earth's core. In: Jacobs, J.A. (Ed.), Geomagnetism, 1st ed. 2. Academic Press, pp. 1–183.

Hammer, M.D., Cox, G.A., Brown, W.J., Beggan, C.D., Finlay, C.C., 2021. Geomagnetic virtual observatories: monitoring geomagnetic secular variation with the swarm satellites. Earth Planets Space 73, 54. https://doi.org/10.1186/s40623-021-01357-9.

Hammer, M.D., Finlay, C.C., Olsen, N., 2022. Secular variation signals in magnetic field gradient tensor elements derived from satellite-based geomagnetic virtual observatories. Geophys. J. Int. 229, 2096–2114. https://doi.org/10.1093/gji/ggac004.

Holme, R., 2015. 8.04 - large-scale flow in the Core. In: Schubert, G. (Ed.), Treatise on Geophysics, Second edition. Elsevier, Oxford, pp. 91–113. https://www.sciencedi

rect.com/science/article/pii/B978044453802400138X. https://doi.org/10.1016/B978-0-444-53802-4.00138-X.
Huder, L., Gillet, N., Thollard, F., 2019. Pygeodyn 1.1.0: a Python package for geomagnetic data assimilation. Geosci. Model Dev. 12, 3795–3803. URL. https://gmd.copernicus.org/articles/12/3795/2019/. https://doi.org/10.5194/gmd-12-3795-2019.
Istas, M., Gillet, N., Finlay, C.C., Hammer, M.D., Huder, L., 2023. Transient core surface dynamics from ground and satellite geomagnetic data. Geophys. J. Int. 233, 1890–1915. https://doi.org/10.1093/gji/ggad039.
Jackson, A., 1997. Time-dependency of tangentially geostrophic core surface motions. Phys. Earth Planet. In. 103, 293–311. URL. https://www.sciencedirect.com/science/article/pii/S0031920197000393. https://doi.org/10.1016/S0031-9201(97)00039-3.
Jault, D., Finlay, C.C., 2015. 8.09 - Waves in the core and mechanical core–mantle interactions. In: Schubert, G. (Ed.), Treatise on Geophysics, Second edition. Elsevier, Oxford, pp. 225–244. URL. https://www.sciencedirect.com/science/article/pii/B9780444538024001500. https://doi.org/10.1016/B978-0-444-53802-4.00150-0.
Jault, D., Gire, C., Le Mouel, J.L., 1988. Westward drift, core motions and exchanges of angular momentum between core and mantle. Nature 333, 353–356. https://doi.org/10.1038/333353a0.
Kloss, C., Finlay, C.C., 2019. Time-dependent low-latitude core flow and geomagnetic field acceleration pulses. Geophys. J. Int. 217, 140–168. https://doi.org/10.1093/gji/ggy545.
Kotsiaros, S., Olsen, N., 2014. End-to-end simulation study of a full magnetic gradiometry mission. Geophys. J. Int. 196, 100–110. https://doi.org/10.1093/gji/ggt339.
Le Mouël, J.L., 1984. Outer-core geostrophic flow and secular variation of Earth's geomagnetic field. Nature 311, 734–735. https://doi.org/10.1038/311734A0.
Livermore, P., Hollerbach, R., Finlay, C., 2017. An accelerating high-latitude jet in Earth's core. Nat. Geosci. 10, 62–68. https://doi.org/10.1038/ngeo2859.
Malin, S.R.C., Hodder, B.M., 1982. Was the 1970 geomagnetic jerk of internal or external origin? Nature 296, 726–728. https://doi.org/10.1038/296726a0.
Mandea, M., Olsen, N., 2006. A new approach to directly determine the secular variation from magnetic satellite observations. Geophys. Res. Lett. 33. https://doi.org/10.1029/2006GL026616.
Mandea, M., Holme, R., Pais, A., Pinheiro, K., Jackson, A., Verbanac, G., 2010. Geomagnetic jerks: Rapid core field variations and core dynamics. Space Sci. Rev. 155, 147–175. https://doi.org/10.1007/s11214-010-9663-x.
Metman, M.C., Livermore, P.W., Mound, J.E., Beggan, C.D., 2019. Modelling decadal secular variation with only magnetic diffusion. Geophys. J. Int. 219, S58–S82. https://doi.org/10.1093/gji/ggz089.
Metman, M.C., Beggan, C.D., Livermore, P.W., Mound, J.E., 2020. Forecasting yearly geomagnetic variation through sequential estimation of core flow and magnetic diffusion. Earth Planets Space 72, 149. https://doi.org/10.1186/s40623-020-01193-3.
Pais, M.A., Jault, D., 2008. Quasi-geostrophic flows responsible for the secular variation of the Earth's magnetic field. Geophys. J. Int. 173, 421–443. https://doi.org/10.1111/j.1365-246X.2008.03741.x.
Pavón-Carrasco, F.J., Marsal, S., Campuzano, S.A., Torta, J.M., 2021. Signs of a new geomagnetic jerk between 2019 and 2020 from Swarm and observatory data. Earth Planets Space 73, 175. https://doi.org/10.1186/s40623-021-01504-2.
Pinheiro, K., Jackson, A., 2008. Can a 1-D mantle electrical conductivity model generate magnetic jerk differential time delays? Geophys. J. Int. 173, 781–792. https://doi.org/10.1111/j.1365-246X.2008.03762.x.
Roberts, P.H., Scott, S., 1965. On analysis of the secular variation — 1. A Hydromagnetic constraint: theory. J. Geomag. Geoelec. 17, 137–151. https://doi.org/10.5636/jgg.17.137.
Ropp, G., Lesur, V., 2023. Mid-latitude and equatorial core surface flow variations derived from observatory and satellite magnetic data. Geophys. J. Int. 234, 1191–1204. https://doi.org/10.1093/gji/ggad113.
Rosat, S., Gillet, N., 2023. Intradecadal variations in length of day: coherence with models of the Earth's core dynamics. Phys. Earth Planet. In. 341, 107053. URL: https://linkinghub.elsevier.com/retrieve/pii/S0031920123000791 https://doi.org/10.1016/j.pepi.2023.107053.
Schwaiger, T., Jault, D., Gillet, N., Schaeffer, N., Mandea, M., 2023. Local estimation of quasi-geostrophic flows in Earth's core. Geophys. J. Int. 234, 494–511. https://doi.org/10.1093/gji/ggad089.
Schwaiger, T., Gillet, N., Jault, D., Istas, M., Mandea, M., 2024. Wave-like motions and torques in Earth's core as inferred from geomagnetic data: a synthetic study. Phys. Earth Planet. In. 346, 107104. https://doi.org/10.1016/J.PEPI.2023.107104.
Suttie, N., Nilsson, A., Gillet, N., Dumberry, M., 2025. Large-scale palaeoflow at the top of Earth's core. Earth Planet. Sci. Lett. 652, 119185. https://doi.org/10.1016/J.EPSL.2024.119185.
Teed, R.J., Jones, C.A., Tobias, S.M., 2019. Torsional waves driven by convection and jets in Earth's liquid core. Geophys. J. Int. 216, 123–129. https://doi.org/10.1093/gji/ggy416.
Torta, J.M., Pavón-Carrasco, F.J., Marsal, S., Finlay, C.C., 2015. Evidence for a new geomagnetic jerk in 2014. Geophys. Res. Lett. 42, 7933–7940. https://doi.org/10.1002/2015GL065501.
Voorhies, C.V., 1993. Geomagnetic estimates of steady surficial core flow and flux diffusion: unexpected geodynamo experiments. In: Dynamics of Earth's Deep Interior and Earth Rotation. Geophysical Monograph Series, pp. 113–125. https://doi.org/10.1029/GM072p0113.
Wardinski, I., Holme, R., Asari, S., Mandea, M., 2008. The 2003 geomagnetic jerk and its relation to the core surface flows. Earth Planet. Sci. Lett. 267, 468–481. https://doi.org/10.1016/J.EPSL.2007.12.008.
Whaler, K.A., 1986. Geomagnetic evidence for fluid upwelling at the core-mantle boundary. Geophys. J. Roy. Astron. Soc. 86, 563–588. https://doi.org/10.1111/j.1365-246X.1986.tb03844.x.
Whaler, K.A., Gubbins, D., 1981. Spherical harmonic analysis of the geomagnetic field: an example of a linear inverse problem. Geophys. J. Roy. Astron. Soc. 65, 645–693. https://doi.org/10.1111/j.1365-246X.1981.tb04877.x.
Whaler, K.A., Olsen, N., Finlay, C.C., 2016. Decadal variability in core surface flows deduced from geomagnetic observatory monthly means. Geophys. J. Int. 207, 228–243. https://doi.org/10.1093/gji/ggw268.
Whaler, K.A., Hammer, M.D., Finlay, C.C., Olsen, N., 2022. Core surface flow changes associated with the 2017 Pacific geomagnetic jerk. Geophys. Res. Lett. 49, e2022GL098616. https://doi.org/10.1029/2022GL098616.
Winch, D.E., Ivers, D.J., Turner, J.P.R., Stening, R.J., 2005. Geomagnetism and Schmidt quasi-normalization. Geophys. J. Int. 160, 487–504. https://doi.org/10.1111/j.1365-246X.2004.02472.x.
Zatman, S., Bloxham, J., 1997. Torsional oscillations and the magnetic field within the Earth's core. Nature 388, 760–763. https://doi.org/10.1038/41987.